FOI-R--0129--SE
June 2001
ISSN 1650-1942

Base data report

Christer Fureby, Magnus Berglund, Eric Lillberg & Gunnar Wijk

Towards the Accurate Simulation of Shock-Waves around Weapon Systems

Weapons and Protection
SE-147 25 TUMBA

SWEDISH DEFENCE RESEARCH AGENCY
Weapons and Protection
SE-147 25 Tumba

FOI-R--0129--SE
June 2001
ISSN 1650-1942
Base data report

Christer Fureby, Magnus Berglund, Eric Lillberg & Gunnar Wijk

Towards the Accurate Simulation of Shock-Waves around Weapon Systems

Issuing organization	Report number, ISRN	Report type
FOI – Swedish Defence Research Agency Weapons and Protection SE-147 25 Tumba	FOI-R--0129--SE	Base data report
	Research area code 4. C4ISR	
	Month year June 2001	Project no. E2002
	Customers code 1. Research for the Government	
	Sub area code 43 Weapons Effect on Humans	

Author/s (editor/s)	Project manager
Christer Fureby Magnus Berglund Eric Lillberg Gunnar Wijk	Gunnar Wijk
	Approved by
	Scientifically and technically responsible Christer Fureby

Report title

Towards the Accurate Simulation of Shock-Waves around Weapon Systems

Abstract (not more than 200 words)

The objective of this study is to examine the evolution of the pressure field around a weapon being fired in order to improve the environment for the operating personnel. When a weapon is fired the propellant burns resulting in a rapid pressure and temperature increase by which the warhead is ejected. Depending on weapon system the shock-waves are of different strength: for a rifle the shooter needs to wear ear plugs in order to avoid hearing impairment, whereas for a howitzer, the personnel also need to wear ear cups. Alternatively, mufflers can be used with marginal effect on the efficiency of the weapon. The most common method of studying pressure around weapons being fired is by means of experiments, but recently also computations, based on first principles, are being carried out. Within the framework of this study, an existing code has been further developed to handle the specific issues pertinent to shock-waves around weapons. Within the framework of this study, this code is validated against a traditional Riemann problem, and later applied to the Swedish PSG 90 rifle. The results are examined with respect to the spatio-temporal evolution of the pressure field and the character of the pressure signal at the shooters position. For simplicity, we have here neglected the effects of the bullet and the volumetric expansion due to exothermicity. We also discuss the possibilities of improving the present computational methodology with the intent of improving it's accuracy and expanding the range of applicability to other weapon systems and to include other effects, such as the effects of exo-thermicity and shock waves produced by the bullet.

Keywords

shock waves around weapons systems, supersonic flow, LES

Further bibliographic information	Language English
ISSN 1650-1942	**Pages** 20 p.
	Price acc. to pricelist Security classification

Utgivare	Rapportnummer, ISRN	Klassificering
Totalförsvarets Forskningsinstitut - FOI Vapen och skydd 147 25 Tumba	FOI-R--0129--SE	Underlagsrapport
	Forskningsområde 4.	
	Månad, år Juni 2001	**Projektnummer** E2009
	Verksamhetsgren 1. Forskning för regeringens behov	
	Delområde 43 Vapeneffekter på människa	

Författare/redaktör	Projektledare
Christer Fureby Magnus Berglund Eric Lillberg Gunnar Wijk	Gunnar Wijk
	Godkänd av
	Tekniskt och/eller vetenskapligt ansvarig Christer Fureby

Rapportens titel (i översättning)

Mot noggranna simuleringar av stötvågor kring vapensystem

Sammanfattning (högst 200 ord)

Syftet med föreliggande studie är att undersöka utvecklingen av tryckfältet kring ett vapen som avfyras för att förbättra miljön för vapenbetjäningen. När ett vapen avfyras brinner krutet vilket ger en snabb ökning av trycket och hastigheten, varmed stridsdelen skjuts ut. Stötvågens styrka beror på vapensystemet: för ett gevär måste skytten bära öronproppar för att undvika hörselskador, medan för en haubits måste betjäningen bära hörselkåpor. Ett alternativ är att använda ljuddämpare med minimal effekt på vapnets effektivitet. Det vanligaste sättet att undersöka tryck kring vapen som avfyras är med hjälp av experiment, men på senare tid har beräkningar, baserade på grundläggande samband, använts. Inom ramen för föreliggande projekt har en befintlig kod utvecklats vidare för att hantera de speciella frågeställningarna av betydelse för stötvågor kring vapen. Dessutom har koden validerats för ett traditionellt Riemannproblem och sedan använts på det svenska PSG 90-geväret. Resultaten har analyserats med avseende på rums- och tidsutvecklingen av tryckfältet och trycksignalens karaktär i skyttens position. För enkelhets skull har vi försummat effekterna av kulan och volymexpansionen på grund av exotermicitet. Vi diskuterar också möjligheterna att förbättra befintlig beräkningsmetodik med avsikten att förbättra dess noggrannhet, att utvidga användningsområdet till andra vapensystem och att innefatta andra effekter, t.ex. effekter av exotermicitet och stötvågen som skapas av kulan.

Nyckelord

stötvågor kring vapensystem, supersonisk strömning, LES

Övriga bibliografiska uppgifter	Språk Engelska
ISSN 1650-1942	**Antal sidor:** 20 s.
Distribution enligt missiv	**Pris: Enligt prislista** **Sekretess**

Contents

Excecutive Summary

The objective of this study is to examine the spatio-temporal evolution of the pressure field around a weapon being fired in order to improve the environment for the operating personnel. When a weapon is fired the propellant burns resulting in rapid pressure and temperature increase by which the warhead is ejected, often at supersonic speeds. A high-speed rifle generates such a strong shock wave that the shooter needs to wear ear protection devises in order to avoid temporary or permanent hearing impairment. Around a heavier weapon, e.g. a howitzer, the personnel need to wear additional ear protection. An alternative way to achieve hearing protection is to utilize mufflers with no or little negative effect on the efficiency of the weapon. The most common method of studying pressure around weapons being fired is by means of experiments, but recently also computations, based on first principles, are being carried out. Calculations of flows with shock waves require massive computational efforts to solve the governing Navier-Stokes Equations. Only recently have such simulations become possible, and opportunities for comparison of computations and experiments have opened up with respect to reducing pressure effects around a weapon, or optimizing pressure effects on a target. Within the framework of this study, computer codes developed for supersonic and hypersonic flows (with other applications in mind) have been further developed in order to handle the specific issues pertinent to the development of shock-waves around weapons. To this end we have carried out two sets of simulations, the first being a straight forward validation study in order to quantify how well the code handles strong propagating shock-waves in an idealized environment. For the second case we have chosen the Swedish rifle PSG 90, which is an adopted version of the British L96A1 or Arctic Warfare (AW). Simulations are performed for conditions with a horizontal barrel located 20 cm above a flat ground. Simulations have been carried out for a muzzle velocity of 1341 m/s corresponding to the sabot rounds used by the Swedish armed forces. Besides analyzing the spatio-temporal evolution of the pressure field we have also investigated the effects on the shooter by means of analyzing the pressure signal at the shooters position. For simplicity, we have here neglected the effects of the bullet and the volumetric expansion due to exothermicity. This is reasonable due to the fact that these effects mainly propagate in the direction of the bullet motion, and do not generally influence the shooter. We also comment on the possibilities of improving the present computational methodology with the intent of improving its accuracy and expanding the range of applicability to other weapon systems and to include other effects, such as the effects of exothermicity and shock waves produced by the bullet.

1. Introduction

Pressure around weapons arises when the weapon is fired and when explosives detonate, which usually occurs close to the target. In the first case the pressure acts on the shooter, which is unwanted, and in the second case it acts on the target. Impact on the shooter is only due to pressure, whilst impact on the target is partly due to pressure and partly due to shrapnel, smoke, radiation, etc. When a weapon is fired the propellant burns less rapidly than when a warhead detonates producing detonation gases. In both cases the gases expand with velocities in excess of the speed of sound in the surrounding air. Hence, a shock wave is created in the surrounding air, which gives a first impact on the objects it hits. Later the combustion and detonation gases, respectively, reach the object and give a second impact. Depending on the size of the charge, the distance to the object or the construction of the object either the first or the second impact may dominate.

The most common method of studying pressure around fired is by means of experiments, using microphones, placed diagonally in front of the muzzle, which register the shock wave from the projectile. This shock wave can be considered as a conical surface with its tip at the nose of the projectile. This front hits the ground behind the projectile, and is reflected as a second shock wave, reaching the microphone with some delay. The amplitude, i.e. the maximum pressure that always occurs at the front of a shock wave, of the reflected wave is lower than that of the primary wave but the persistence is presumably greater. Still later, a third shock wave occurs, which is generated when the combustion gases flow out of the gun muzzle after the projectile. If the microphone is placed close enough, the amplitude and the duration of this wave are considerably greater that those of the primary and secondary waves. Thus, when the objective is to determine the pressure effects on personnel in the vicinity of the gun the third wave is most important. A prerequisite for the third shock wave to be computed is that it is well separated in time form the first and second waves. In practice, this is obtained at relatively small distances from the muzzle. Simulations of shock waves that hit a microphone shall in principle be carried out in such a manner that the reflections from the surrounding equipment and from the ground as well as from the pressure registration surface of the microphone itself are accounted for. The microphones around a weapon are normally placed where the crew has their heads during firing. When people are present around the weapon, their bodies can be represented as surfaces against which shock waves are reflected. Accordingly, the measured pressure and the actual pressure during operation are different, but this may be compensated for in the comparison of measured and simulated pressure.

Calculation of shock waves requires massive computational efforts to solve the coupled non-linear partial differential equations, which govern these processes, i.e. the Navier-Stokes Equations (NSE), [1]. Similar systems of equations govern the expansion of the combustion and detonation gases, which generates the shock waves in air. Only recently have such simulations become possible, and opportunities for comparison of computations and experiments have opened up with respect to e.g. reducing pressure effects around a weapon being fired, or optimizing pressure effects on a target. In the present investigation only the first aspect is considered, and we focus on simulating only the third wave. The reason for this is that computer codes of this kind do not usually solve problems involving moving boundaries. There is nothing in principle that hinders the development of codes able to handle moving boundaries, but a considerable effort is required and the computational effort will be prohibitive for some time. In supersonic flow turbulence and shock waves compete in defining the smallest flow structures. Turbulence produces a cascade of eddies ranging in size from the integral scales λ_I to the smallest Kolmogorov scales λ_K. The ratio of the largest to the smallest eddy scales is related to the Reynolds number $Re=u\lambda/\nu$, where u is a charac-

teristic velocity, λ a characteristic length and ν the molecular viscosity, i.e. $\lambda_l/\lambda_K=Re^{3/4}$, [2]. This implies that the degrees of freedom (i.e. the number of grid points) required in Direct Numerical Simulations, [3], in which all scales are resolved, scale as $Re^{9/4}$. For high Re-number flows, present-day computers are not powerful enough to handle such problems and thus alternative methods have to be developed for turbulent flows. A further complication arises in compressible flows where shocks and discontinuities are transformed into sharp but continuous profiles due to viscosity and heat conduction. Consequently, an internal structure over the shock-thickness λ_S occurs, conditioned by the balance between viscous and thermal effects. Often both λ_K and λ_S are too small to be resolved by the grid (having a spacing $\Delta>\lambda_K$) and therefore, neither the internal turbulent nor shock structures will be explicitly computed unless alternative simulation models are adopted that can faithfully represent their effects on the larger resolved flow structures.

Turbulence modeling methods generally start by distinguishing between a 'mean' component and a fluctuating component which is associated with the unresolved flow, [4]. In the commonly used Reynolds Averaged Navier-Stokes (RANS) methods, [5], the starting point is an ensemble average of the flow (sometimes time-averaging or averaging over homogeneous directions are used) to derive the RANS equations. The RANS equations are then solved together with models for the Reynolds stress tensor to represent the influence of the turbulence. In Large Eddy Simulation (LES) methods, [6], an explicit or implicit spatial filtering operation is applied to separate the large-scale resolvable flow from the small-scale flow. Filtering the NSE provides a set of equations of the large-scale flow that must be supplemented with models describing the effects of the small subgrid flow on the resolvable flow. Since the filter width is based on the grid spacing, the components are referred to as grid scale and subgrid scale (SGS) components, respectively. Partitioning the flow in this way means that some parts of the flow (the large eddies) are simulated explicitly. Moreover, LES hold the promise of providing further information about the flow, since LES simulates the dynamics of the large-scale flow, including the intermediate scale turbulence. LES is also potentially more accurate, [7], since the LES-equations being solved are closer in form to the NSE, which they reduce to when the mesh is refined, which is not the case for RANS.

The objective of the simulations of pressure around weapons aims at ensuring that the operating personnel are unharmed when the weapon is used. A high-velocity rifle generates such strong shock waves that the firing soldier needs to wear ear protection devices in order to avoid temporary or permanent hearing impairment. Around a heavier weapon, e.g. a howitzer, the personnel may need also to wear additional ear protection. An alternative way to achieve hearing protection is to develop mufflers for weapons, with marginal effect on the efficiency of the weapon. In the aforementioned experiments mufflers were also used. A microphone diagonally in front of the gun muzzle registered the same primary and secondary shock waves as when no muffler was used, but the third shock wave was in this case reduced to negligible level compared to the other two shocks waves. It is possible that a systematic development of mufflers for weapons is both more efficient and cheaper to prevent hearing impairment than the (presumably) dominating research efforts to improve hearing protection devices. The development of mufflers may be hastened and more efficient using computations, as described in this report.

The report is outlined as follows: chapter 2 describes the computational methods used including physical modeling and numerical methods; chapter 3 describes the results of a simple validation study, i.e. a shock-tube problem, and chapter 4 describes the results when the simulation model is applied to investigate the pressure around a PSG 90 rifle. In chapter 5 we summarize the results and give some suggestions and recommendations for future studies.

2. The Computational Approach

The fluid dynamic model used is based on partial differential equations describing conservation of mass and balance of momentum and energy for a Newtonian fluid, [1], viz.,

$$\begin{cases} \partial_t(\rho)+\mathrm{div}(\rho\mathbf{v})=0, \\ \partial_t(\rho\mathbf{v})+\mathrm{div}(\rho\mathbf{v}\otimes\mathbf{v})=-\mathrm{grad}p+\mathrm{div}\mathbf{S}+\rho\mathbf{f}, \\ \partial_t(\rho E)+\mathrm{div}(\rho E\mathbf{v})=\mathrm{div}\mathbf{h}+\mathrm{div}((-p\mathbf{I}+\mathbf{S})\mathbf{v})+\rho\sigma, \end{cases} \tag{1}$$

where ρ is the density, $\mathbf{v}$ the velocity, p the pressure, $\mathbf{S}$ the stress tensor, $\mathbf{f}$ the body force (assumed negligible for high Ma and Re-number flows), E the total energy, $\mathbf{h}$ the heat flux vector, $\mathbf{I}$ the identity tensor and σ the non-mechanical net-power (usually assumed negligible for non-reacting flows). The total energy E is defined as the sum of the internal energy e and the kinetic energy $\frac{1}{2}|\mathbf{v}|^2$ so that $E=e+\frac{1}{2}|\mathbf{v}|^2$. The balance equations (1) are supplemented by constitutive equations and thermodynamic laws describing the influence of pressure, internal energy, fluid stresses and heat fluxes on the variables ρ, $\mathbf{v}$ and T. For a Newtonian fluid in thermodynamic equilibrium the stress tensor $\mathbf{S}$ is represented by the viscous stress tensor $\mathbf{S}=\lambda(\mathrm{tr}\mathbf{D})\mathbf{I}+2\mu\mathbf{D}$, where μ and λ are the viscosity coefficients, $\mathbf{D}=\frac{1}{2}(\mathbf{L}+\mathbf{L}^T)$ the rate-of-strain tensor and $\mathbf{L}=\mathrm{grad}\mathbf{v}$ the velocity gradient tensor. Up to now, with the expectation of high temperature or pressure, there is no experimental evidence that Stokes relation $3\lambda+2\mu=0$ is not satisfied, and thus we may simplify the constitutive equation for $\mathbf{S}$ so that $\mathbf{S}=2\mu\mathbf{D}_D$, where $\mathbf{D}_D=\mathbf{D}-\frac{1}{3}(\mathrm{tr}\mathbf{D})\mathbf{I}$ denotes the deviatoric part of $\mathbf{D}$. The heat flux vector $\mathbf{h}$ is generally assumed to follow Fourier's law of heat conduction $\mathbf{h}=\kappa\mathrm{grad}T$, where κ is the thermal conductivity. In addition, the variation of μ and κ is given as functions of the fluid state, for instance of temperature. For gases, particularly air, a widely used relation for the dynamic viscosity is given by Sutherland's formula $\mu=\alpha_1 T^{3/2}/(T+\alpha_2)$ and similarly for the thermal conductivity, which may be expressed as $\kappa=\beta_1 T^{3/2}/(T+\beta_2)$. Appropriate values for the parameters α_i and β_i may be obtained from the open literature, e.g. [8].

The thermodynamic equations of state define the functional dependence of pressure and internal energy on the remaining variables, i.e. $p=p(\rho,T)$ and $e=e(\rho,T)$. Often a compressible fluid can be considered a perfect gas, even if viscous effects are taken into account and the equations of state are $p=\rho RT$ and $e=\int_{T_0}^{T} c_V dT$, where R is the gas constant per unit of mass being equal to the universal gas constant divided by the molecular mass whilst c_V is the specific heat coefficient for constant volume. Because of the hypersonic nature of the flow we include the temperature dependence of c_V, i.e. $c_V=c_V(T)$, that usually can be expressed in polynomial form as $c_V=a+bT+cT^{-2}$, where a, b and c are experimentally determined coefficients. We also introduce the ratio $\gamma=c_P/c_V$ of specific heat coefficients under constant pressure c_p and constant volume c_V so that $c_P=c_V+R$. The Mach-number is hereafter defined as $\mathrm{Ma}=|\mathbf{v}|/c$, where $c^2=(\partial p/\partial\rho)_S=\gamma RT=\gamma p/\rho$ is the square of the speed of sound. For high-speed flows peak pressures are commonly in excess of 10 atm, at which compressibility effects starts to become important. When a fluid is being compressed, the molecules are brought closer together, and the effects of the intermolecular interaction become increasingly important, involving not only attractive (long-range) forces but also repulsive (short range) forces. To account for this we introduce a compressibility factor $\sigma=\sigma(\rho,T)$ so that $p=\sigma\rho RT$, which recovers the equation of state for an ideal gas when $\sigma=1$. A common method to describe the compressibility is through a virial development, [9], in which $\sigma=1+f(\rho b)$ where b is the covolume and f denotes the functional dependence. For this study, we have used the Boltzmann equation of state $p=\sigma\rho RT$, [10], with $\sigma=1+\rho b(1+\rho b(0.625+\rho b(0.287+\rho b(0.193))))$.

The presence of viscosity and heat conduction transforms the momentum and energy equations into second-order partial differential equations. Hence, in the unknowns **v** and E, these equations are parabolic in time and hyperbolic-parabolic in space. The continuity equation (1_1) is hyperbolic in both space and time since it remains a first order differential equation for the density ρ. The NSE is thus a hybrid system being hyperbolic-parabolic in space and time. In LES, the motion is separated into small and large scales and equations are solved for the latter. The partition is achieved by means of applying a low-pass filter $G=G(\mathbf{x},\Delta)$ to the NSE, viz.,

$$\begin{cases} \partial_t(\bar{\rho})+\mathrm{div}(\bar{\rho}\tilde{\mathbf{v}})=m^{\rho}, \\ \partial_t(\bar{\rho}\tilde{\mathbf{v}})+\mathrm{div}(\bar{\rho}\tilde{\mathbf{v}}\otimes\tilde{\mathbf{v}})=-\mathrm{grad}\bar{p}+\mathrm{div}\bar{\mathbf{S}}-\mathrm{div}\mathbf{B}+\mathbf{m}^{v}, \\ \partial_t(\bar{\rho}\tilde{E})+\mathrm{div}(\bar{\rho}\tilde{E}\tilde{\mathbf{v}})=\mathrm{div}\bar{\mathbf{h}}+\mathrm{div}((-\bar{p}\mathbf{I}+\bar{\mathbf{S}})\tilde{\mathbf{v}})-\mathrm{div}\mathbf{b}+m^{E}, \end{cases} \tag{2}$$

where overbars denote filtered variables and tildes Favré filtered variables. As a result of the filtering the SGS stress tensor $\mathbf{B}=\bar{\rho}(\widetilde{\mathbf{v}\otimes\mathbf{v}}-\tilde{\mathbf{v}}\otimes\tilde{\mathbf{v}})$ and flux vector $\mathbf{b}=\bar{\rho}(\widetilde{\mathbf{v}e}-\tilde{\mathbf{v}}\tilde{e})+(\overline{p\mathbf{v}}-\bar{p}\tilde{\mathbf{v}}+\bar{\mathbf{S}}\tilde{\mathbf{v}}-\overline{\mathbf{S}\mathbf{v}})$ emerge, representing effects of the unresolved flow on the resolved flow, [6]. Furthermore, the commutation error terms m^{ρ}, $\mathbf{m}^{v}$ and m^{E} are generally non-zero, and result from the inability to change order between low-pass filtering and differentiation, i.e. $m^{f}=[G*,\nabla]f=\overline{\nabla f}-\nabla\bar{f}\neq 0$ for an arbitrary variable f. The commutation error terms are generally neglected, but may also be amalgamated into the SGS terms div**B** and div**b** before attempts are made to model them. These SGS terms should be modeled using information from the resolved flow, prior to discretization at a spatial resolution near Δ, typically more affordable than DNS, which requires resolution near the Kolmogorov scale $\lambda_K<\Delta$. In the absence of a universal theory of turbulence the development of SGS models must include rational use of empirical data. Modern SGS models includes algebraic and one-equation eddy-viscosity models, scale similarity models and differential stress models and models developed in some adjoint space such as the Eddy-Damped Quasi-Normal Markovian and Structure Function models, e.g. [11] and references therein. More recently however, other types of LES models have been suggested, e.g. Monotone Integrated LES (MILES), [12], combining high-resolution schemes with implicit filters to provide built-in or implicit SGS models, or LES models based on homogenisation using multiple-scales expansion methods, [13].

For the purpose of this study the MILES approach is adopted. MILES is based essentially on two properties of the equations to be solved and the physics they describe: (i) the conceptual interpretation of turbulence as composed of thin filaments of intense vorticity embedded in a setting of weak vorticity, [14], or in more general terms that the SGS flow structure consists of sharp but continuous variation in the dependent variables; and (ii) the observation that any discretisation acts as a filter on the scale of the grid spacing Δ, [15]. One advantage of MILES over conventional LES (described above) is that the commutation error terms do not appear since the filter is implicit to the differential operators. As compared to conventional LES, where effects of the SGS flow on the resolvable flow are modeled by explicit SGS models, MILES uses the intrinsic properties of high-resolution schemes, [16], to construct implicit (i.e. built-in) SGS models by means of the leading order truncation error, [17], having properties close to those of the explicit SGS models. In a finite volume (FV) setting this is accomplished by splitting the the computational domain D into cells Ω_P so that $\cup_P(\Omega_P)=D\cup\partial D$ and $\cap_P(\Omega_P)=\emptyset$ and integrating the NSE (1) over $D\cup\partial D$. By introducing local averages, i.e. $f_P=\frac{1}{\delta V_P}\int_{\Omega_P} f\,dV$, Gauss theorem may be used to obtain the semi-discretised MILES equations. The cell-averaging is the implicit counterpart in MILES to the explicit low-pass filtering

in LES, and the kernel is typically of top-hat shape. By integrating the resulting ordinary differential equations in time using multi-step methods, [16], the discretized MILES equations are

$$\begin{cases} \sum_{i=0}^{m}(\alpha_i \rho_P^{n+i} + \frac{\beta_i \Delta t}{\delta V_P}\sum_f [F_f^{C,\rho}]^{n+i}) = 0, \\ \sum_{i=0}^{m}(\alpha_i (\rho \mathbf{v})_P^{n+i} + \frac{\beta_i \Delta t}{\delta V_P}\sum_f [\mathbf{F}_f^{C,v} + \mathbf{F}_f^{D,v} + \mathbf{F}_f^{2,v}]^{n+i}) = -\beta_i (\mathrm{grad}p)_P^{n+i}\Delta t, \\ \sum_{i=0}^{m}(\alpha_i (\rho E)_P^{n+i} + \frac{\beta_i \Delta t}{\delta V_P}\sum_f [F_f^{C,E} + F_f^{D,E} + F_f^{1,E} + F_f^{W,E}]^{n+i}) = 0, \end{cases} \tag{3}$$

where m, α_i and β_i are parameters of the time-integration scheme, and

$$\begin{cases} F_f^{C,\rho} = (\rho \mathbf{v}\cdot d\mathbf{A})_f, \;\; \mathbf{F}_f^{C,v} = (\rho \mathbf{v}\cdot d\mathbf{A})_f \mathbf{v}_f, \;\; F_f^{C,E} = (\rho \mathbf{v}\cdot d\mathbf{A})_f E_f, \\ \mathbf{F}_f^{D,v} = (\mu \mathrm{grad}\mathbf{v})_f d\mathbf{A}, \;\; \mathbf{F}_f^{2,v} = (\mu \mathrm{grad}\mathbf{v}^T)_f d\mathbf{A}, \\ F_f^{D,E} = (\frac{\kappa}{C_v}\mathrm{gradE})_f \cdot d\mathbf{A}, \;\; F_f^{1,E} = (\frac{\kappa}{C_v}\mathrm{grad}|\mathbf{v}|^2)_f \cdot d\mathbf{A}, \;\; F_f^{W,E} = ((-p\mathbf{I}+\mathbf{S})\mathbf{v})_f \cdot d\mathbf{A}, \end{cases} \tag{4}$$

are the convective, viscous and diffusive and supplementary fluxes involved in the continuity, momentum and energy equations. To complete the FV-discretization all fluxes, defined at cell faces f, need to be reconstructed from values of the dependent variables at adjacent cells. This requires flux interpolation for the convective fluxes and difference approximations to the inner derivatives in the viscous and diffusive and supplementary fluxes. With the aim of achieving second-order accuracy, the discretization of the inner derivatives in the viscous, diffusive and additional fluxes is carried out using central differencing. To illustrate this, consider the viscous flux in (4_2), discretized by $\mathbf{F}_f^{D,v} = \mu|d\mathbf{A}|(\mathbf{v}_N - \mathbf{v}_P)/|\mathbf{d}| + \frac{1}{6}\mu(\mathbf{d}\otimes\mathbf{d})\nabla^3\mathbf{v}$, where $\frac{1}{6}\mu(\mathbf{d}\otimes\mathbf{d})\nabla^3\mathbf{v}$ is the leading order (dispersive) truncation error. The functional reconstruction of the convective fluxes involves interpolation using adjacent-cell values, e.g. $\mathbf{F}_f^{C,v} = (\rho \mathbf{v}\cdot d\mathbf{A})_f \mathbf{v}_f \approx F_f^{C,\rho}\mathbf{v}_f$, where the flux-function $\mathbf{v}_f = \mathbf{v}_f(\mathbf{v}_P, \mathbf{v}_N)$ still needs to be specified whilst the flux $F_f^{C,\rho}$ can be provided from the discretized momentum equation (4_2) using face interpolation. The specification of $\mathbf{v}_f = \mathbf{v}_f(\mathbf{v}_P, \mathbf{v}_N)$ is coupled to the properties of the scheme and the leading order truncation error. The scheme should comply with the physical principles of causality, monotonicity and positivity, and therefore it must be non-linear, [18], and the most consistent way of deriving such a scheme is by using flux-limiters. The flux limiter Γ is introduced as to combine a high-order flux-function $\mathbf{v}_f^H$, that is well-behaved in smooth regions, with a low-order (dispersion-free) flux-function $\mathbf{v}_f^L$, that is well-behaved near sharp gradients, so that we may write $\mathbf{v}_f^L$, i.e. $\mathbf{v}_f = \mathbf{v}_f^H - (1-\Gamma)[\mathbf{v}_f^H - \mathbf{v}_f^L]$. Typically, $\mathbf{v}_f^H$ is obtained from a linear approximation whilst $\mathbf{v}_f^L$ is obtained from an upwind biased, piecewise constant approximation. More precisely,

$$\begin{cases} \mathbf{v}_f^H = \mathtt{l}\mathbf{v}_P + (1-\mathtt{l})\mathbf{v}_N - \frac{1}{8}(\mathbf{d}\otimes\mathbf{d})\nabla^2\mathbf{v}, \\ \mathbf{v}_f^L = \beta^+\mathbf{v}_P + \beta^-\mathbf{v}_N + (\beta^+ - \beta^-)(\nabla\mathbf{v})\mathbf{d}; \;\; \beta^\pm = \frac{1}{2}(\mathbf{v}_f\cdot d\mathbf{A} \pm |\mathbf{v}_f\cdot d\mathbf{A}|)/|\mathbf{v}_f\cdot d\mathbf{A}|, \end{cases} \tag{5}$$

where $\mathtt{l}$ is the distance function and $-\frac{1}{8}(\mathbf{d}\otimes\mathbf{d})\nabla^2\mathbf{v}$ and $(\beta^+ - \beta^-)(\nabla\mathbf{v})\mathbf{d}$ represent the leading order truncation errors. The flux limiter is to be formulated as to allow as much as possible of the correction or antidiffusion term $[\mathbf{v}_f^H - \mathbf{v}_f^L]$ to be included without violating the principles of causality, monotonicity and positivity. Although the choice of flux limiters is not easy the intrinsic properties of these are well-known, i.e. Γ must be a positive function of the ratios of consequtive variations in the dependent variables and it should only deviate from unity in regions where the variable is close to an extermum or has sharp gradients. Several limiters exist that satisfy these conditions with the most appropriate limiters for MILES probably being the FCT limiter of Boris & Book, [19], generalized by Zalesak, [20], and the recent GAMMA limiter of Hjasak, [21].

In order to investigate the MILES model we study the modified differential equations. These may be obtained as the discretized equations are assembled, simply by recognizing the discretized forms of the operators and including the leading order truncation errors, viz.,

$$\begin{cases} \partial_t(\rho)+\mathrm{div}(\rho\mathbf{v})=0, \\ \partial_t(\rho\mathbf{v})+\mathrm{div}(\rho\mathbf{v}\otimes\mathbf{v})=-\mathrm{grad}p+\mathrm{div}\mathbf{S}+\mathrm{div}(\rho(\mathbf{C}\mathbf{L}^{\mathrm{T}}+\mathbf{L}\mathbf{C}^{\mathrm{T}}+\chi^2\mathbf{L}\mathbf{d}\otimes\mathbf{L}\mathbf{d})+\tfrac{1}{6}\mu(\mathbf{d}\otimes\mathbf{d})\nabla^3\mathbf{v}+\ldots), \\ \partial_t(\rho E)+\mathrm{div}(\rho E\mathbf{v})=\mathrm{div}\mathbf{h}+\mathrm{div}((-p\mathbf{I}+\mathbf{S})\mathbf{v})+\mathrm{div}(\rho(\mathbf{C}\nabla E+\chi^2\nabla E\otimes\mathbf{d})+\tfrac{1}{6}\kappa(\mathbf{d}\otimes\mathbf{d})\nabla^3 E+\ldots), \end{cases} \tag{6}$$

where $\mathbf{C}=\chi(\mathbf{v}\otimes\mathbf{d})$ and $\chi=\frac{1}{2}(1-\Gamma)(\beta^{-}-\beta^{+})$. As compared to the raw NSE (1) the discretisation has introduced additional dissipative and dispersive terms, from which we identify the implicit or built-in SGS terms as $\mathbf{B}=\rho(\mathbf{C}\mathbf{L}^{\mathrm{T}}+\mathbf{L}\mathbf{C}^{\mathrm{T}}+\chi^2\mathbf{L}\mathbf{d}\otimes\mathbf{L}\mathbf{d})$ and $\mathbf{b}=\rho(\mathbf{C}\nabla E+\chi^2\nabla E\otimes\mathbf{d})$. The implicit SGS stress tensor can be split into $\mathbf{B}^{(1)}=\rho(\mathbf{C}\mathbf{L}^{\mathrm{T}}+\mathbf{L}\mathbf{C}^{\mathrm{T}})$ and $\mathbf{B}^{(2)}=\rho\chi^2(\mathbf{L}\mathbf{d}\otimes\mathbf{L}\mathbf{d})$, of which the former is a generalized eddy-viscosity model with $\mathbf{C}$ being the tensor-valued eddy-viscosity, whilst the latter is of a form similar to the scale similarity part in the Bardina model, [22]. This decomposition is attractive also considering the decomposition into rapid and slow parts suggested by Shao et al, [23]. In MILES, the rapid part that cannot be captured by isotropic SGS models relates to $\mathbf{B}^{(2)}$ and $\mathbf{b}^{(2)}$, whilst the slow part relates to $\mathbf{B}^{(1)}$ and $\mathbf{b}^{(1)}$. Furthermore, Borue & Orszag, [24], have shown that $\mathbf{B}^{(2)}$ improves the correlations between the exact and modeled SGS stress tensor.

To decouple the pressure-velocity system a Poisson equation for the pressure is derived from the discretized continuity and momentum equations, (3_1) and (3_2), viz.,

$$\tfrac{\Delta t}{\delta V_P}\textstyle\sum_f\left[\left(\frac{1}{a_P}\right)_f(\mathrm{grad}p)_f^{n+m}\cdot d\mathbf{A}\right]=\tfrac{\Delta t}{\delta V_P}\sum_f\left[\left(\frac{1}{a_P}\mathbf{L}[\rho,\mathbf{v}]\right)_f\cdot d\mathbf{A}\right]-\delta_t(\rho)\Delta t, \tag{7}$$

where $\mathbf{L}[\rho,\mathbf{v}]=\sum_N[a_N(\rho\mathbf{v})_N^{n+m}]-\mathbf{S}(\rho,\mathbf{v})$, and where a_P and a_N denote the matrix coefficients for P and the neighbors N, respectively, and $\mathbf{S}(\rho,\mathbf{v})$ represents all source terms apart from the pressure gradient. The set of equations is solved sequentially with iteration over the explicit coupling terms to get rapid convergence. The segregated approach results in a Courant number restriction. A maximum Co-number of 0.5 gives satisfactory stability and accuracy but a value of 0.2 is preferable, since in LES we aim at resolving the motion of the smallest resolved eddies.

3. The Shock Tube Problem

The shock tube problem (or the Riemann problem) constitutes a particularly interesting test case, since it presents an exact solution to the full system of one-dimensional Euler equations (obtained from the NSE by neglecting the molecular viscosity and the heat conductivity) containing simultaneously a shock wave, a contact discontinuity and an expansion fan. From this particular problem much can be learnt about the propagation of shock waves and discontinuities. It can be realized experimentally by the sudden breakdown of a diaphragm in an infinitely long virtually one-dimensional tube, separating initial gas states at different pressures and densities. Figure 1 shows schematically the shock tube problem. After the bursting of the diaphragm, at t=0, the pressure discontinuity propagates to the right in the low-pressure gas and simultaneously an expansion fan propagates to the left in the high-pressure gas. Moreover, a contact discontinuity separating the two gas regions propagates to the right in the tube. Since the shock and contact discontinuities move in regions of uniform conditions, they will do so with constant velocity, and the expansion is centered

at the diaphragm position $(x,t)=(x_0,0)$. Figure 2 shows the characteristics and discontinuities evolution in space and time.

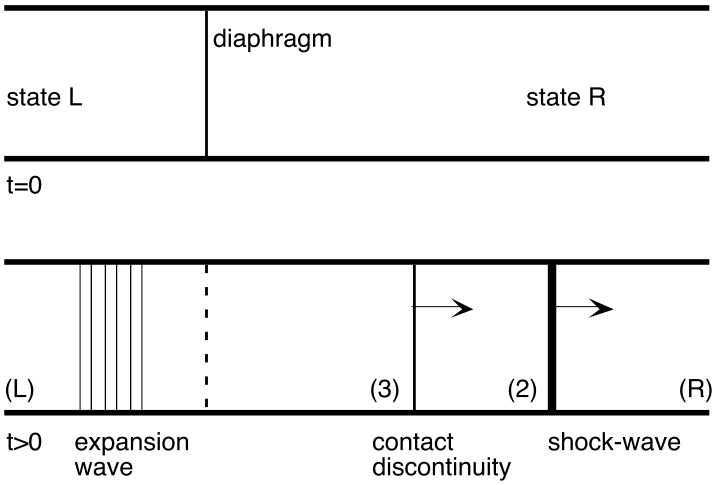

Figure 1. Schematic presentation of the shock tube or Riemann problem. At t=0 the initial condition consists of the two states L and R separated by a diaphragm.

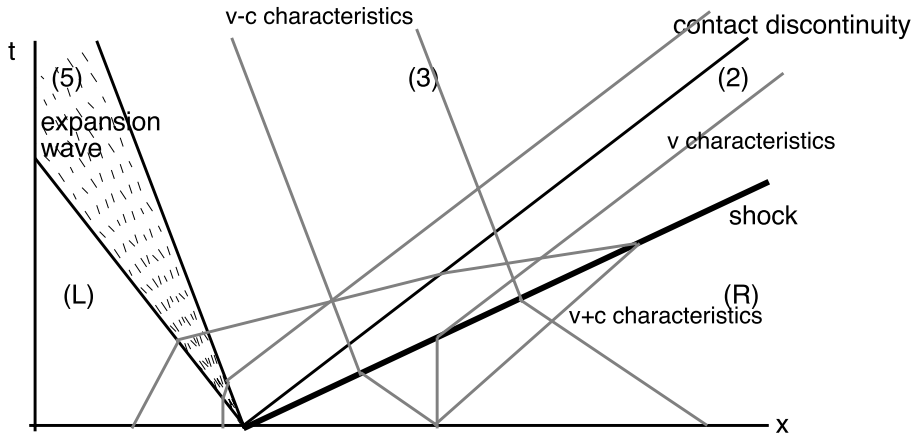

Figure 2. Characteristics and discontinuities originating at the interface between the two gas states (L and R) in the shock tube or Riemann problem.

We usually distinguish between region R containing undisturbed gas at low-pressure p_R, region 2 containing the disturbed low-pressure gas, region 3 containing the disturbed high-pressure gas, region L containing the undisturbed gas at the high-pressure p_L and region 5 (the so-called expansion fan) containing gas through which the pressure and all other variables vary continuously. A shock-wave separates region R from region 2 and a contact discontinuity separates region 2 from region 3. The disturbed high-pressure region (region 3) is in turn influenced by the expansion fan (region 5) propagating to the left into the undisturbed high-pressure region (region L). Analytical expressions describing the variation of all dependent variables can be obtained rather easily, and are presented in many textbooks on computational fluid dynamics, especially those having a pronounced numerical inclination, e.g. [25-26]. Here we use this test case to validate the simulation model used to simulate shock-waves around weapons systems and other supersonic flow cases. To this end we consider the following two sets of initial conditions:

- $p_L=10^5$, $\rho_L=1$, $p_R=10^4$, $\rho_R=0.125$ and $v_L=v_R=0$,

- $p_L=10^5$, $\rho_L=1$, $p_R=10^3$, $\rho_R=0.010$ and $v_L=v_R=0$,

of which the first case (case I) corresponds to an initial pressure ratio of $Q_I=10$ whereas the second case (case II) corresponds to an initial pressure ratio of $Q_{II}=100$. The test data corresponds to those used by Sod, [27]. Figure presents the variation of pressure, axial velocity and Mach (Ma) number in the shock tube or Riemann problem at t=6.1 ms for (3a) case I and (3b) case II.

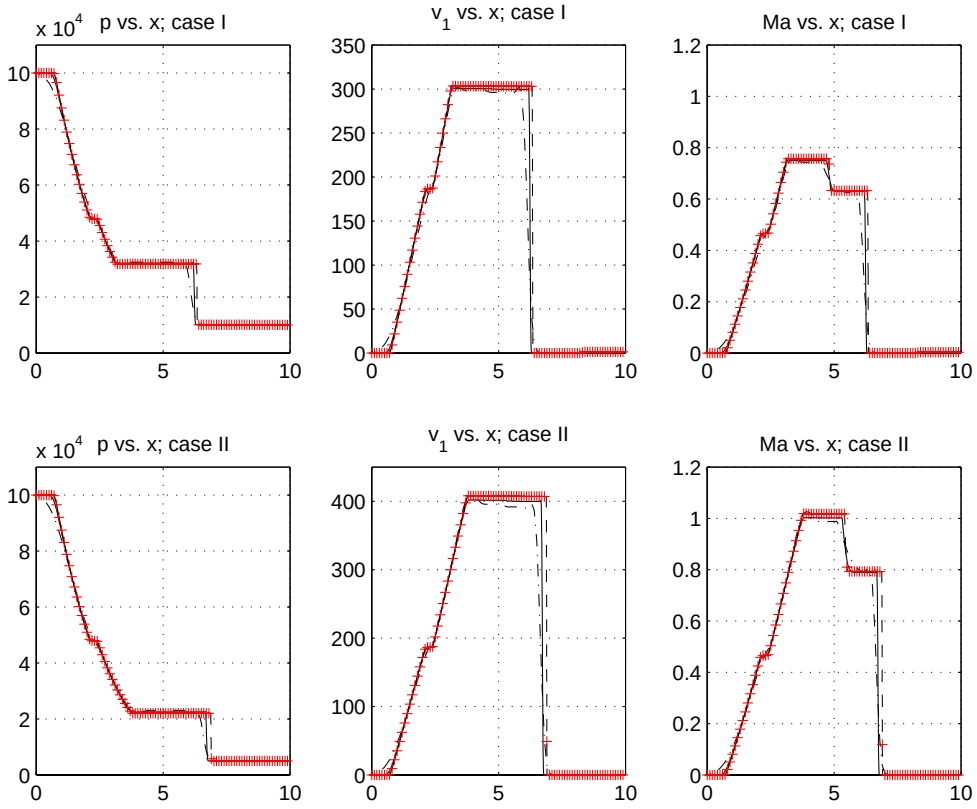

Figure 3. Variation of typical flow quantities in the shock tube for (a) case I and (b) case II. The left panel shows pressure, the middle panels shows Ma-number whilst the right panels shows velocity. Legend: (--·-·-) $\Delta x=L/100$, (—) $\Delta x=L/1000$ and (- - -) $\Delta x=L/10000$.

In case I the shock pressure ratio is moderate ($Q_S\approx3$), while case II corresponds to a strong shock with $Q_S\approx7$, and supersonic Ma-numbers following the expansion fan. Looking at the Ma-number evolution from right to left, the first discontinuity is caused by the shock wave propagating downstream, followed by the contact discontinuity. By studying the other curves it is seen that the shock wave corresponds to discontinuous variations of all the variables including entropy, while velocity and pressure are continuous over the contact discontinuity. Upstream of the contact discontinuity the smooth variation represents the expansion waves. Observe also the linear variation of the velocity in the expansion region and its isentropic nature. As can be seen, the numerical simulations using the MILES model capture all major features of the flow, and do not give rise to any spurious oscillations in the vicinity of any discontinuities. In fact, the scheme used in the present study is better than most other schemes developed for hypersonic flows. The influence of the spatial resolution is surprisingly weak, with the coarser grids resulting in smoother shock profiles, as caused by the higher numerical diffusivity discussed previously.

4. Simulation of Shock-Waves around a PSG 90 Rifle

In order to simulate the spatio-temporal evolution of the flow around a weapon system used in the Swedish armed forces we have chosen the rifle PSG 90, which is an adopted version of the British L96A1, or Arctic Warfare (AW), figure 4. There are a few differences in the two rifles, mainly in the length of the barrel and the twist. The caliber is 7.62 NATO, the overall length is 1.15 m, with a barrel length of 0.66 m. The weight is 6.7 kg in ready condition. The magazine capacity is 9 rounds and the maximum effective range is 900 m. The AW series of rifles has a very good reputation and is being adopted in military applications around the world. The Swedish armed forces applied a sabot round, with a tungsten carbide projectile. With this modification the rounds exit the barrel at about 1300 m/s at a pressure of about 20 MPa. The rifle can be equipped with a bipod and in this particular configuration, with the barrel in horizontal position, the barrel is about 20 cm above the ground, which is the configuration to be simulated.

Figure 4. The Swedish PSG 90 rifle.

The computational domain and the location of the barrel are presented in figure 5 together with the coordinate system used. The computational domain consists of a hemi-cylindrical domain with an overall length of eight barrel lengths (L=0.66 m) and a radius of two barrel lengths. The muzzle is located in the middle of the computational domain 20 cm above the horizontal ground. To apply the

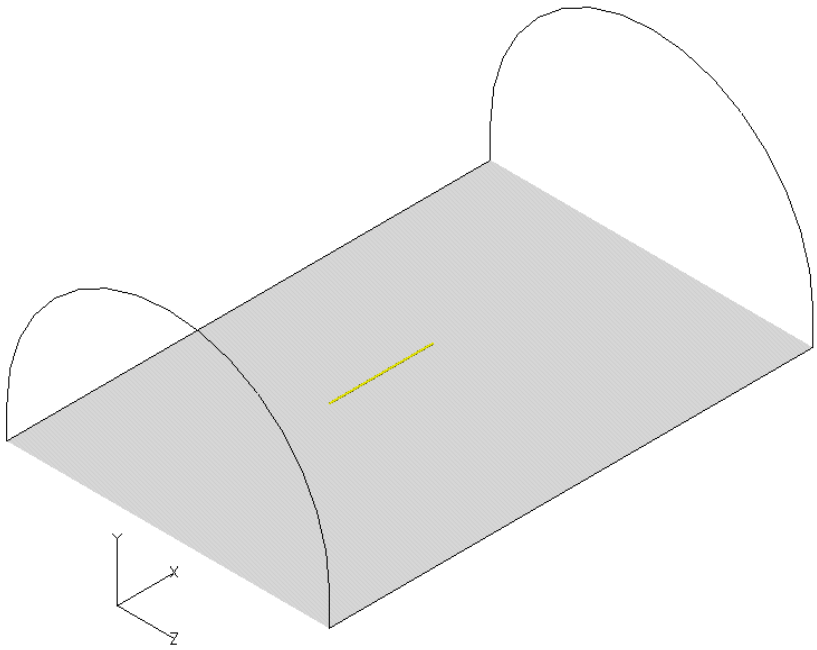

Figure 5. Schematic of the computational domain and the coordinate system used in the PSG 90 simulations. The barrel (yellow) is located in the middle of the computational domain.

finite volume discretization of the governing equations (2) or (3-4) the computational domain, i.e. the volume between the barrel and the outer edge, must be divided into a network of small topological hexahedra, see figure 6. Optimal performance of the solvers, minimization of the leading order truncation error and accurate shock-capturing require the network of hexahedra to be as uniform as possible at the same time as being concentrated to flow regions with strong gradients or rapid variations in the dependent variables. To handle this without resorting to adaptive grid generation, which often results in degradation of solver performance or lack of accuracy, quite some effort is spent on optimizing the grid quality in terms of stretching, warpage and skewness. High-order schemes are well-known to give best results on uniform hexahedra, although research is underway to improve this performance orf arbitrary-shaped polyhedra meshes.

The grid is shown in figure 6 and consists of about 200 k cells, and is clustered towards the gun muzzle in order to resolve as much as possible of the initial shock-wave and the associated shear layers. The initial conditions consist in specifying the pressure, temperature and velocity of the gas within the barrel at an instant just after the bullet has left the muzzle. The values are p=20 MPa, T=750 K and v=1341 m/s, and are obtained from a conventional estimate based on the performance characteristics of the weapon. Outside of the barrel normal temperature and pressure conditions are assumed together with zero freestream velocity. The detonation gases are assumed to have the following properties $M=25\cdot10^{3}$ kg/mol, $c_p=1250$ J/(K·kg), $\mu=50\cdot10^{-6}$ kg/(m·s), $\gamma=1.40$, and $\kappa=75\cdot10^{-6}$ (kg·m)/(s^3·K). The boundary conditions at the ground are $\mathrm{gradE}\cdot\mathbf{n}=0$, $\mathrm{gradp}\cdot\mathbf{n}=0$ and $\mathbf{v}=0$, where **n** is the unit normal direction of the ground, implying that the ground is modeled as a fully reflective, adiabatic, no-slip surface. The boundary conditions of the gun barrel are **v**=**0**,

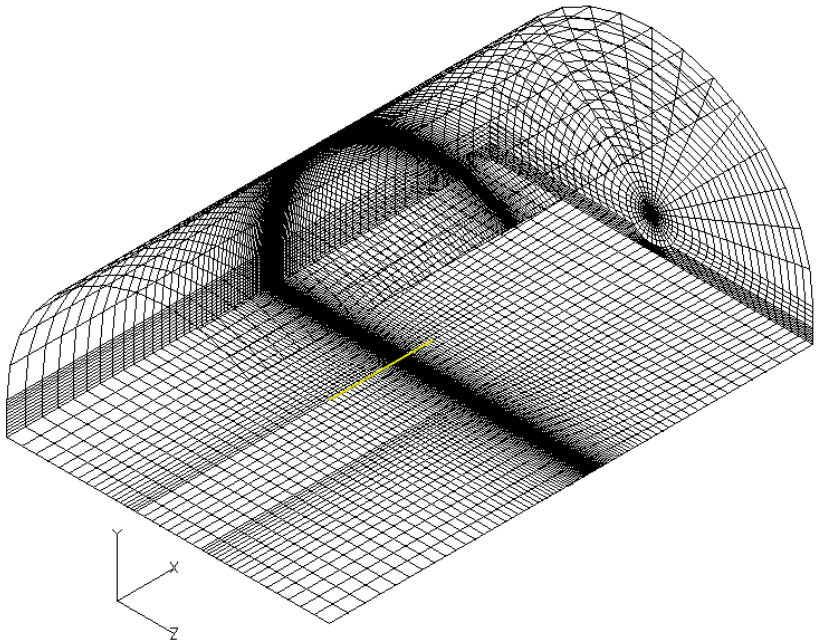

Figure 6. Schematic representation of the computational grid used in the PSG 90 simulations.

$\mathrm{gradp}\cdot\mathbf{n}=0$ and $\mathrm{gradE}\cdot\mathbf{n}=0$, where **n** is the normal direction of the barrel. At the far-field boundaries of the computational domain we use a wave transmissive boundary condition, similar to that of Poinsot & Lele, [28], in order to dampen reflections from outward traveling pressure and entropy waves. Previous investigations have shown that this boundary condition dampens about 95% of the amplitude of the outward traveling waves. For cases in which a large number of characteristic times (e.g. flow-through times) are required this may not be sufficient, so that other methods have

to be used. However, for the case considered here we are only looking at short times and therefore no reflections from the far-field boundaries reach the central part of the computational domain, which is the part considered here. The boundary conditions are consistent with the conditions obtained from characteristic analysis of the NSE.

Figure 7 shows a time sequence of the pressure in the vicinity of the barrel in the centerplane. The left boundary of each panel corresponds to the rear end of the barrel, i.e. close to the position of the shooters ear. As already mentioned, the length of the barrel is 66 cm and the barrel is located 20 cm above the ground, which assumed to be perfectly flat. In figure 7a we see detonation gases starting to exit and expand from the gun muzzle, forming a hemisphere with the peak pressure opposite the muzzle. Within the interior of the hemisphere a low-pressure region is formed. However, this will probably not be the case in a real situation due to continued combustion of the detonation gases. In a future study the effect of combustion will be included. Later, in figure 7b, the detonation gases have expanded further and are now starting to interact with the ground causing the reflection seen in figure 7c. At this stage the hemispheric pressure field is starting to deform, and the low pressure region is completely separated into two bubbles – one moving upwards and the other moving downwards. At this stage we can also see a more complex pattern of alternating high and low-pressure regions starting to form outside of the gun muzzle. At the same time the outer edges of the high-pressure region have moved backwards and are now just ahead of the shooter. Note that the shooter will experience the impact of both the upper and lower branches, at about the same time. In figure 7d the hemispheric high-pressure structure is completely broken, with the lower branch interfering with the ground resulting in a local high-pressure region together with damping and higher energy dissipation due to friction (i.e. shear) with the ground. This increases the asymmetry of the high-pressure region, and causes this to change direction upwards. The low-pressure core has formed a toroidal structure, with its lower branch just reaching the ground. Secondary and tertiary structures are being formed in the vicinity of the gun muzzle and the barrel. Figures 7e to 7f show the continuation of this process in which the high-pressure region increases its width due to the combined effects of physical and numerical dissipation. The shape of the high-pressure region is also somewhat altered due to its interaction with the ground and the advection effects. In figure 7g we notice that the shooter now experiences a second high-pressure pulse, caused by the secondary structures mentioned earlier. In figure 7h the high-pressure region is seen to rapidly loose its coherence and intensity. Alternating pressure maxima and minima can bee seen to travel upstream of the barrel to reach the shooter at an instant about 5.0 ms after figure 7h. The physical

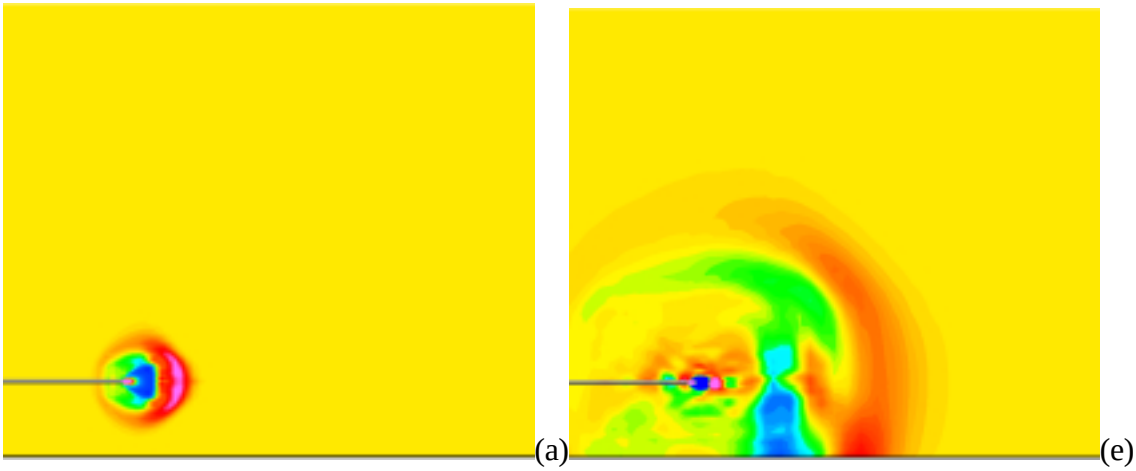
(a) (e)

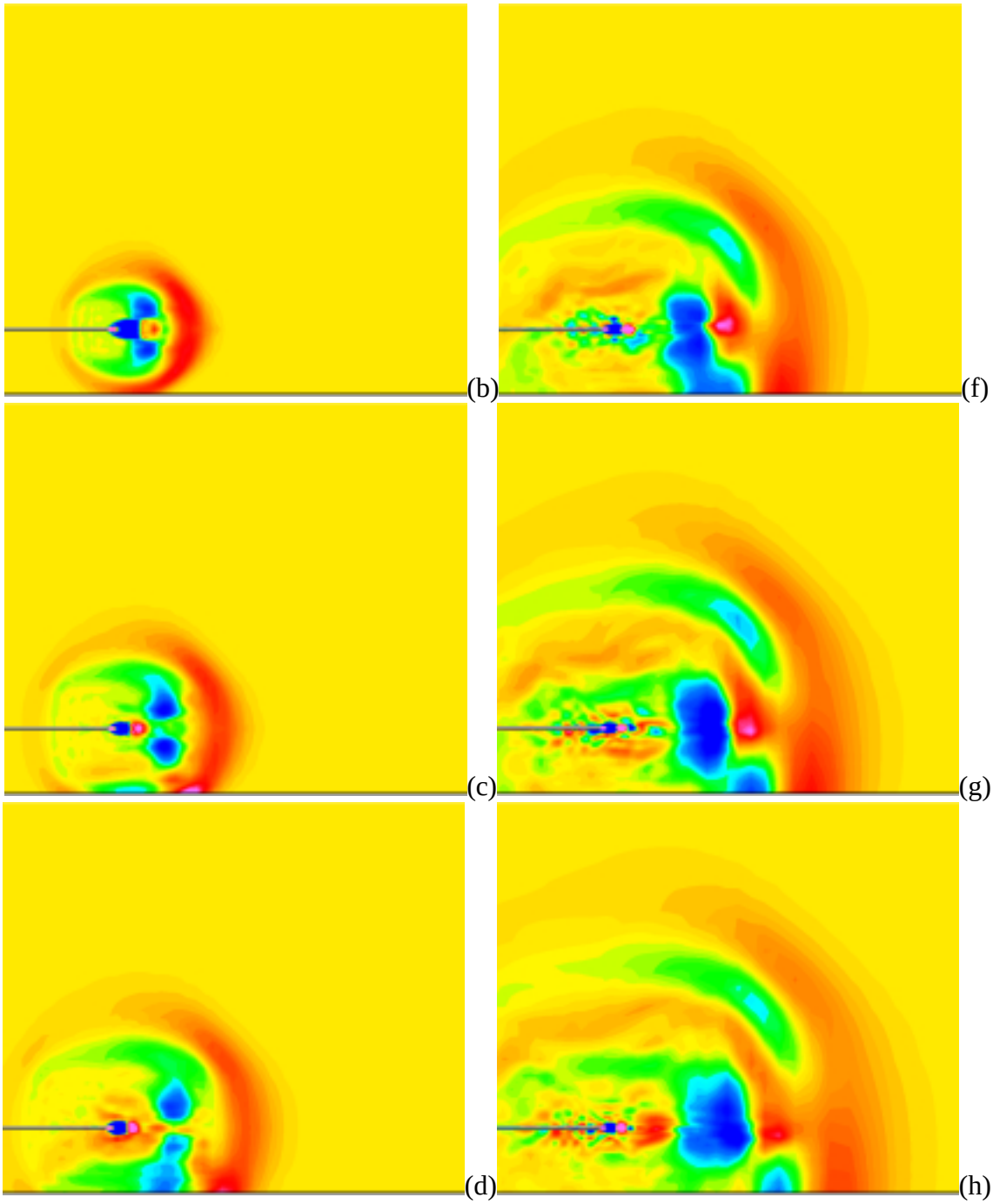

Figure 7. Time-sequence from the side of the flow-field evolving from the gun-muzzle in terms of pressure contours. Figure 7a is about 5 ms after the gun is fired, and there is 5.0 ms between each of the subsequent figures.

character in the results described is qualitatively correct, but it is likely that we underestimate the strength of the shock wave and overestimate its width. It is also possible that some small scale structures, or structures that are dependent on small scale effects (e.g. associated with the reflection) are not captured in the simulation due to the fairly coarse grid. In a future study a heavily refined grid will be used to try to resolve more of the shock-wave dynamics. In conjunction with this we will also incorporate the effects of secondary combustion occurring just outside of the gun muzzle. It is likely that the secondary combustion affects the dynamics of the entire pressure and flow field due to exothermicity effects, not accounted for in this simulation. Figure 8 presents a snapshot of the pressure at the ground at a time corresponding to that of figure 7f. From figure 7

and figure 8, the three-dimensionality and associated complexity of the pressure field is evident. Hence, three-dimensional simulations with high spatial resolution are required if qualitatively and quantitatively accurate results are required. It is also evident from figure 8 that the shooter will experience also the high-pressure branches from the sides. There will be a time lap between the high-pressure pulses from below and from the sides due to the reflection from the ground. This is likely to reduce the maximum pressure, since these pressure peaks will not occur simultaneously. On the other hand, the pressure-gradient distribution will be much more complicated due to this.

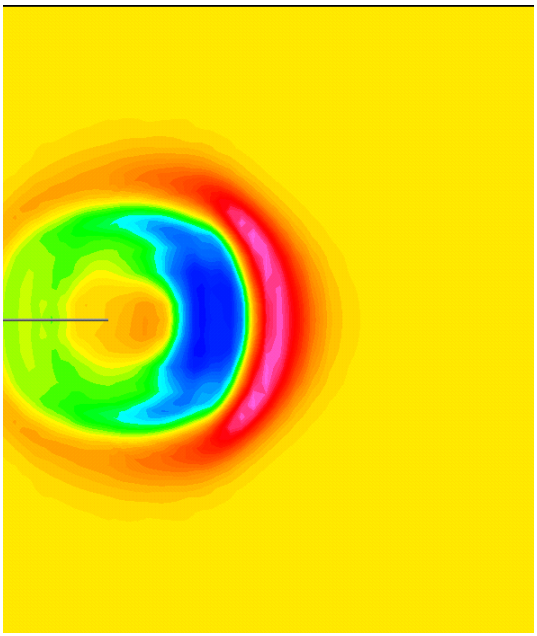

Figure 8. Pressure contours at the ground corresponding to figure 7f.

Figure 9 shows the pressure signal at the approximate location of the shooters head. It is beyond the scope of this work to discuss the physiological effects of the pressure field on the human ear (or body in general) but some general comments will still be made. As a reference we notice that the lowest sound pressure that a human can hear is $2 \cdot 10^{-5}$ Pa, and the highest that a human ear can withstand without physical pain is $2 \cdot 10^{2}$ Pa. The most intense sounds is therefore 10^{7} times higher than the weakest sound. The human ear does not react lineraly, but rather logaritmically, and therefore the strongest sounds are not experienced as 10^{7} times more intense than the weakest. A suitable measure is obtained by the sound pressure level $I_p = 20 \cdot \log(p/p_{ref})$, where $p_{ref} = 20 \cdot 10^{-5}$ Pa is a reference pressure. Based on the results in figure 9 we estimate that the first peak has a sound pressure level of 176 dB and the highest sound pressure level during the presented time window is 196 dB. The durations of these pressure pulses are however very short, in general less than 0.2 ms, and the acoustic power is therefore low. It is clear that the sound pressure levels are high enough to be able to cause temporary or permanent damage to the human ear, this however, is also strongly affected by the acoustic power and the frequency contents of the acoustic signal.

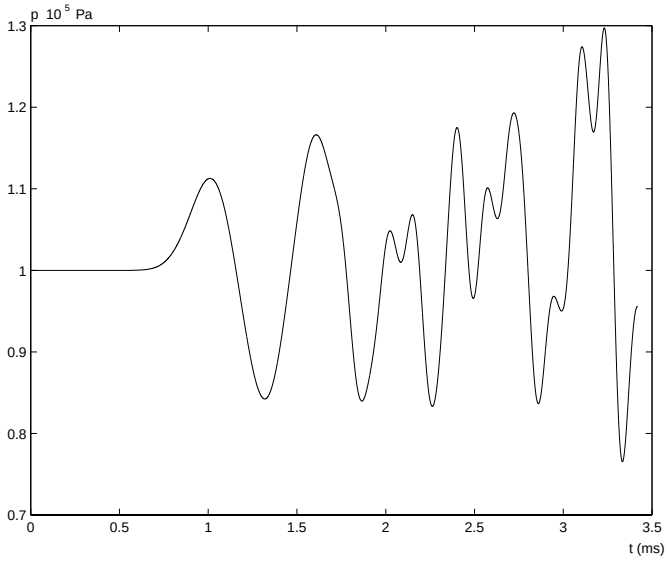

Figure 9. The pressure signal at the approximate location of the shooters head.

5. Concluding Remarks

The aim of this study is to examine the pressure and the associated flow around a weapon being fired in order to improve the environment for the operating personnel. Depending on weapon the shock-waves are of different strength: for a rifle the shooter needs to wear ear plugs to avoid hearing impairment, whereas for a heavier weapon the personnel need to wear additional ear protection. The most common method of investigating such problems is by means of experiments, but recently, computations, based on first principles, are being carried out. Within the framework of this study, an existing code has been further developed to handle the specific issues pertinent to shock waves around weapons. The code has been validated against a shock tube problem with very good results, indicating that the numerical methods are capable of handling shock-waves and other discontinuities when the grid is sufficiently fine. To demonstrate the capabilities of the method, we have made preliminary calculations around a PSG 90 rifle using a fairly coarse mesh in order to (i) obtain general information about the flow and the resolution requirements, (ii) examine the characteristic time and length scales of the problem, and (iii) to study the feasibility of a performing a sufficiently resolved calculation. The problem is further simplified, and the calculations perfomed thus suffer from the following drawbacks:

- too low spatial resolution, which manifests itself in smearing of shock-waves and discontinuities together with masking of small scale flow features. Preliminary two-dimensional simulations with higher resolution give an indication of the resolution required, but cannot be used to investigate the flow physics due to the development of unphysical flow features due to two-dimensional effects.
- lack of secondary combustion effects, which are belived to be important in the early stages of the development of the pressure mainly due to exothermicity effects,
- the assumption that the bullet does not affect the secondary pressure.

The results obtained show qualitatively reasonable results, and give an indication of how much information that can be extracted from a three-dimensional time-dependent simulation. Suffiently resolved three-dimensional simulations will have the answer to many of the complex, and yet poorly understood phenomena, observed in the measurements.

References

[1] Lions P.L.; 1996, “Mathematical Topics in Fluid Mechanics”, Oxford Science Publications, Oxford.

[2] Frisch U.; 1995, “Turbulence”, Cambridge University Press.

[3] Leonard A.; 1996, “Direct Numerical Simulation of Turbulent Flows“, in Simulation and Modeling of Turbulent Flows Eds. Gatski T.B., Hussaini M.Y. & Lumeley J.L. Oxford University Press, New York.

[4] Reynolds W.C.; 1990, “The Potential and Limitations of Direct and Large Eddy Simulations” in Wither Turbulence? Turbulence at the Crossroads, ed. Lumley J.L., Lecture Notes in Physics, **357**, Springer Verlag, p 313.

[5] Launder B.E.; 1996, “An Introduction to Single Point Closure Methodology“, in Simulation and Modeling of Turbulent Flows Eds. Gatski T.B., Hussaini M.Y. & Lumeley J.L. Oxford University Press, New York.

[6] Lesieur M & Metais O; 1996, “New Trends in Large Eddy Simulations of Turbulence”, Annu. Rev. Fluid Mech., **28**, p 45.

[7] Fureby C. & Tabor G.; 1997, “Mathematical and Physical Constraints of Large Eddy Simulations”, J. Theor. and Comp. Fluid Dyn., **9**, p 85.

[8] Bird R.B., Stewart W.E. & Lightfoot E.N.; 1960, “Transport Phenomena”, J. Wiley & Sons, New York.

[9] Atkins P.W.; 1987, “Physical Chemistry”, Oxford University Press, 3rd Ed.

[10] Bauer p. & Brochet C.; 1983, “Properties of Detonation Waves in Hydrocarbon-oxygen-nitrogen Mixtures at High Initial Pressures”, AIAA Progress in Aero Astro, **87**, p 231.

[11] Metais O. & Lesieur M.; 1992, “Spectral Large Eddy Simulation of Isotropic and Stably Stratified Turbulence”, J. Fluid Mech., **239**, p 157.

[12] Boris J.P., Grinstein F.F., Oran E.S. & Kolbe R.J.; 1992, “New Insights into Large Eddy Simulation”, Fluid Dyn. Res., **10**, p 199.

[13] Fureby C.; 1999, ”Homogenisation by Multiple Scales Expansion of the Navier Stokes Equations”, FOA-R--99-01291-310--SE.

[14] Kuo A.Y. & Corrsin S.; 1971, “Experiment on the Geometry of the Fine-structure Regions in Fully Developed Turbulent Fluid”, J. Fluid Mech., **56**, p 447.

[15] Ghosal S, & Moin P.; 1995, “The Basic Equations for the Large Eddy Simulation of Turbulent Flows in Complex Geometry“, J. Comp. Phys., **118**, p 24.

[16] Hirsch C.; 1999, “Numerical Computation of Internal and External Flows”, J. Wiley & Sones.

[17] Fureby C. & Grinstein F.F.; 1998, “Large Eddy Simulation of High Reynolds Number Free and Wall Bounded Flows”, Submitted to J. Comp. Phys.

[18] Godunov S.K.; 1959, “A Difference Method for Numerical Calculation of Discontinuous Solutions of the Equations of Hydrodynamics”, Mat. Sb., **47**, p 271.

[19] Boris J.P. & Book D.L.; 1973, “Flux Corrected Transport I, SHASTA, a Fluid Transport Algorithm that Works”, J. Comp. Phys. **11**, p 38

[20] Zalesak S.; 1979, “Fully Multidimensional Flux-Corrected Transport Algorithms for Fluids”, J. Comp. Phys., **31**, p 335.

[21] Jasak H.; 1997, “Error Analysis and Estimation for the Finite Volume Method with Application to Fluid Flows”, PhD thesis, Imperial College, London, UK.

[22] Bardina J., Ferziger J.H. & Reynolds W.C.; 1980, “Improved Subgrid Scale Models for Large Eddy Simulations”, AIAA Paper No. 80-1357.

[23] Shao L., Sarkar S. & Pantano C.; 1999, “On the Relationship Between the Mean Flow and Subgrid Stresses in Large Eddy Simulation of Turbulent Shear Flows”, Phys. Fluids, **11**, p 1229.

[24] Borue V. & Orszag, S.A.;1998, “Local Energy Flux and Subgrid-Scale Statistics in Three Dimensional Turbulence”, J. Fluid Mech., **366**, p 1.

[25] Fletcher C.A.J.; 1992, “Computational Methods in Fluid Dynamics”, Springer-Verlag, Berlin and New York.

[26] LeVeque R.J.; 1992, “Numerical Methods for Conservation Laws”, 2nd Ed., Birkhüser Verlag, Berlin

[27] Sod G.A.; 1978, “A Survey of Several Finite Difference Methods for Systems of Non-linear Hyperbolic Conservation Laws”, J. Comp. Phys., **27**, p 1.

[28] Poinsot T.J. & Lele S.K.; 1992, “Boundary Conditions for Direct Simulation of Compressible Viscous Reacting Flows”, J. Comp. Phys., **101**, p 104.